

Accepted Manuscript

Joining of carbon fiber reinforced thermoplastic and metal via friction stir welding with co-controlling shape and performance

Yongxian Huang, Xiangchen Meng, Yuming Xie, Junchen Li, Long Wan

PII: S1359-835X(18)30255-0
DOI: <https://doi.org/10.1016/j.compositesa.2018.06.027>
Reference: JCOMA 5088

To appear in: *Composites: Part A*

Received Date: 19 April 2018
Revised Date: 8 June 2018
Accepted Date: 20 June 2018

Please cite this article as: Huang, Y., Meng, X., Xie, Y., Li, J., Wan, L., Joining of carbon fiber reinforced thermoplastic and metal via friction stir welding with co-controlling shape and performance, *Composites: Part A* (2018), doi: <https://doi.org/10.1016/j.compositesa.2018.06.027>

This is a PDF file of an unedited manuscript that has been accepted for publication. As a service to our customers we are providing this early version of the manuscript. The manuscript will undergo copyediting, typesetting, and review of the resulting proof before it is published in its final form. Please note that during the production process errors may be discovered which could affect the content, and all legal disclaimers that apply to the journal pertain.



Joining of carbon fiber reinforced thermoplastic and metal via friction stir welding with co-controlling shape and performance

Yongxian Huang*, Xiangchen Meng, Yuming Xie, Junchen Li, Long Wan

State Key Laboratory of Advanced Welding and Joining, Harbin Institute of Technology,

Harbin 150001, China

*Corresponding author: Email: yxhuang@hit.edu.cn (Tel. +86-451-86413951; Fax +86-451-86416186;)

Abstract: Short carbon fiber reinforced poly-ether-ether-ketone (SCF/PEEK) and 2060-T8 aluminum alloy (AA2060-T8) were joined via friction stir welding with co-controlling shape and performance. The high-quality surface integrity and joint formation were acquired based on a tapered thread pin with the triple facets, a stationary shoulder and a new lap configuration of the SCF/PEEK and the AA2060-T8 at the upper and lower sides. An intimate contact formed at the AA2060-T8 and the SCF/PEEK interface. The macro/micro-mechanical interlocking and the chemical bond attributed to the main bonding mechanisms. Decreasing heat input was beneficial to eliminating the welding defects and improving the load bearing of the joint. The maximum tensile shear strength was 33 MPa. This work indicates that friction stir welding with co-controlling shape and performance has the feasible and potential to join thermoplastic and metal.

Keywords: Joints/joining; Polymer-matrix composites (PMCs); Hybrid; Mechanical properties.

1. Introduction

Global trends in CO₂ emission and gas price have attracted extensive attentions from

the manufacturing fields of automotive, aerospace, and so on, to produce the lighter, safer and more environmental friendly vehicles [1]. The selection of light materials, such as aluminum (Al) alloy and thermoplastic, can reduce the structural weight. Joining of the hybrid structure with metal and thermoplastic is inevitable. Requirements of complex surface treatments and long curing time for adhesive bonding as well as stress concentration and weight penalty correlated with mechanical fastening motivate for new joining methods [2–4]. The state-of-the-art ultrasonic welding [5,6], laser welding [7] and friction spot welding (FSpJ) [8,9] are restricted due to the types of polymer matrix composites and the geometries of workpieces.

Friction stir welding (FSW) has the huge advantage to join metal and thermoplastic polymer due to low peak temperature and severe plastic deformation [10]. Liu et al. [11] utilized friction lap welding (FLW), that only has a rotational shoulder, to join monomer casting nylon (MC Nylon-6) and 6061-T6 Al alloy. Nagatsuka et al. [12] joined carbon fiber reinforced thermoplastic to 5052 Al alloy via FLW based on the hydrogen bonding induced by oxidation film. However, the bubbles at the metal/polymer interface decreased tensile shear properties. Welding tool of friction stir lap welding (FSLW) contains a rotational shoulder and a rotational pin. Ratanathavorn et al. [13] employed FSLW to join 6111 Al alloy and poly-phenylene-sulphide (PPS) at the upper and lower sides. They stated that mechanical interlocking attributed to tensile shear properties. Shahmiri et al. [14] adopted FSLW to join 5052 Al alloy and poly-propylene (PP) by a thread pin, while a coarse surface appearance containing polymer and Al alloy pieces was achieved. Derazkola et al. [15] achieved a relatively coarse joint surface based on

poly-methyl-methacrylate (PMMA) and 5058 Al alloy at the upper and lower sides. Welding tool is the core of FSLW. The material transfer induced by the rotation of the rotational pin influences the mechanical interlocking and joint integrity. Panneerselvam et al. [16] reported a good joint formation was obtained by a taper thread pin for FSW of PP. Payganeh et al. [17] discussed that a triangle thread pin produced the large contacting area with the welded workpieces, and obtained good joint formation. In previous study, a tapered thread pin with the triple facets was also beneficial to fabricating an Al anchor and improving the mechanical interlocking [18].

In the present study, from the viewpoints of joint surface integrity and strength, friction stir welding with co-controlling shape and performance was proposed to join carbon fiber reinforced thermoplastic and metal. The friction stir welding with co-controlling shape and performance can also provide a technical support to join thermoplastic and metal. Joint integrity, microstructural evolution, interface characteristic and mechanical properties of the hybrid joint were investigated in detail.

2. Experimental procedure

The adherends were short carbon fiber reinforced poly-ether-ether-ketone (SCF/PEEK) sheet with a thickness of 3 mm and 2060-T8 Al alloy (AA2060-T8) sheet with a thickness of 2 mm. A welding tool system contained a stationary shoulder, a rotational shoulder and a tapered thread pin with the triple facets. The outer and inner diameters of the stationary shoulder were 12 mm and 8.5 mm. The diameters of the rotational shoulder, the pin bottom and top were 8 mm, 5 mm and 3 mm, respectively. The length of the rotational pin was 3.2 mm. Schematic of friction stir welding with

co-controlling shape and performance between the SCF/PEEK and the AA2060-T8 is displayed in Fig. 1. Rotational velocities varied from 1400 rpm to 2000 rpm with the increment of 200 rpm. A welding speed of 30 mm/min was fixed. A plunging depth and a tilting angle with respect to Z-axis were 0.2 mm and 2.0° , respectively.

Microstructural and mechanical specimens were cut perpendicular to the welding direction by a water jet cutter with reference of DIN EN 1465:2009 [19], as exhibited in Fig. 2. The metallographic specimens were polished by different grades of emery papers (400#, 800#, 1200#, 2000#, 3000#, 5000# and 7000#), while the final polishing was performed by the diamond compounds ($1.5\ \mu\text{m}$) in the disc polishing machine. The microstructural specimens were observed by an optical microscope (OM) and a scanning electron microscope (SEM) with an energy dispersive X-ray spectroscopy (EDS). A very thin gold layer was coated for the SEM observation by a fully automated argon ion polishing system (Gatan 685) at a dwell time of 10 min. A constraint fixture was fabricated and employed to guarantee the accuracy of the tensile shear test. Schematic of the auxiliary fixture during the tensile shear test is exhibited in Fig. 3 [8]. During tensile shear test, the tensile shear specimen was fixed by the auxiliary fixture and binding bolts, which guaranteed that the specimen only bore the force along the tensile shear direction and then avoided the occurrence of the torsion. Three shear tensile specimens were prepared to evaluate the tensile shear properties, as shown in Fig. 2. The tensile shear tests were performed at room temperature at a constant crosshead speed of 1 mm/min. Since the shear tensile test results were only reported as a load-displacement curve by a test machine, the joining area was achieved by observing the macrostructures. Therefore, the

maximum tensile shear force divided by the joining area was used for the calculation of the tensile shear strength. Moreover, fracture energy was calculated according to the area underneath the load-extension curve until the maximum fracture force is achieved [8,20]. Fracture surfaces of the tensile shear specimens were observed by SEM. Vickers microhardness tests were performed with a load of 50 g and a dwell time of 10 s for AA2060-T8, and a load of 10 g and a dwell time of 15 s for PEEK.

3. Results and discussion

3.1 Surface integrity

Fig. 4 displays the favorable surface integrity of the typical joint based on the novel welding mode containing the stationary shoulder and the tapered thread pin with triple facets as well as the new configuration that the SCF/PEEK locates at the upper of the AA2060-T8. A coarse surface formation containing fragmentized Al or polymer pieces by the past configuration that the metal locates at the upper of polymer is successfully eliminated. A good surface finishing can be achieved at a rational process window, in which the flashes and shoulder marks with concave troughs and convex crests are eliminated. The influencing factors are attributed to the following three aspects. Firstly, compared with the past configuration (metal at the upper side and polymer at the lower side) reported by the Ratanathavorn et al. [13] and Shahmiri et al. [14], the lower AA2060-T8 in this work, as a backing plate, can provide the sufficient plunging force on the upper SCF/PEEK and then produce the higher frictional heat. The rotational pin contacts with the lower AA2060-T8, which easily generates the frictional heat to soften

the PEEK near the interface between the AA2060-T8 and the SCF/PEEK, and then recoups the heat loss at the bottom of the SCF/PEEK sheet induced by a low thermal conductivity. These synthesis effects guarantee the welding heat input. Next, the tapered thread pin with the triple facets has the more pulses per sec compared with a conventional tool such as a taper or thread pin [21]. With the rotation and advancement of the new rotational tool, the plasticized materials flow along the surface of the rotational pin, which transforms the AA2060-T8 flow into the SCF/PEEK, and then improves the mixture of the both materials. Finally, the stationary shoulder is still not rotating and locates at the outer of the rotational tool. These phenomena effectively prevent the softening SCF/PEEK overflowing out of the stir zone (SZ), and control the joint integrity.

Fig. 5 displays the three-dimensional surface morphologies of the joints at different rotational velocities. At a rotational velocity of 1400 rpm, an unfilled defect appears on the joint surface due to the brittle materials induced by insufficient frictional heat (Fig. 5a). When rotational velocity is 1600 rpm, the frictional heat and material transfer are enhanced. These improvements are beneficial to driving the plasticized materials under the space between the welding tool and its surrounding hard materials, eliminating the unfilled defect (Fig. 5b). For the rotational velocity of 1800 rpm or 2000 rpm, high frictional heat increases the spreading of the polymer. This phenomenon results in the overflowing out of the joint from the gap between the stationary shoulder and the rotational tool, causing the partial unfilled defect (Figs. 5c and d).

3.2 Microstructure

Fig. 6 depicts the microstructures in cross-section of the hybrid joints at different

rotational velocities. The loss of plasticized materials induced by an unreasonable welding process window exerts significant influence on the microstructures. A defect-free joint is obtained at an optimized welding window. The AA2060-T8 at the lower side penetrates into the SCF/PEEK at the upper side and mixes together due to the material transfer induced by the rotation of the rotational tool, in which an Al anchor forms and is responsible for mechanical interlocking, and consequently contributing to the joint strength. The rotation of the thread pin transforms the plasticized Al materials to flow upwards along the thread of the rotational pin. The Al materials down-bend and penetrate into the lap intersection since the SCF/PEEK is easily softened, and further lead to the formation of the Al anchor (Fig. 6). The SZ is filled with the Al particles or pieces characterized by the orange particles in Fig. 6. For conventional FSW of thermoplastic polymer, a kissing bond defect easily appears at the retreating side (RS) due to the difference of shear stress between the RS and the advancing side (AS), decreasing the tensile properties [22]. In the study, the formation of the Al anchor with high heat is beneficial to softening the SCF/PEEK and forming the adhesion between the Al anchor and the SCF/PEEK, which effectively avoid the kissing bond. With the increase of rotational velocity, the height of the Al anchor gradually decreases in general. At a rotational velocity of 1400 rpm, the largest Al anchor in width and height can be acquired. For the lap configuration in this study, the SCF/PEEK at the upper side is difficult to transfer the frictional heat generated by the rotational shoulder from the top to the lower sheet due to the low thermal conductivity of the SCF/PEEK ($0.92 \text{ K/m}^{-1}\text{k}^{-1}$). Therefore, only the partial rotational pin contacts with the AA2060-T8 and then produces low

frictional heat, resulting in the largest Al anchor. Meanwhile, the low frictional heat results in the insufficient material transfer and then a cavity defect forms at the bottom of the SZ, as displayed in Fig. 6a. With increasing rotational velocity to 1600 rpm, the enhancement of frictional heat improves the transfer of the plasticized materials, which can eliminate the cavity defect (Fig. 6b). As the rotational velocities further increase to 1800 rpm and 2000 rpm, the sizes of the Al anchor of the hybrid joints decrease (Figs. 6c and d). This is attributed to that the relatively high frictional heat and the good material flow can transform the softening thermoplastic polymer flow into the bottom of the SZ, which prevents the plasticized Al alloy deeply penetrating into the upper sheet, and then results in the small Al anchor. Especially, the Al anchor at the RS is smaller than that at the AS. This is attributed to that the peak temperature at the AS is higher than that at the RS, and then results in the insufficient plasticized materials at the RS. It can be postulated that the mechanical interlocking between the plasticized AA2060-T8 and the re-solidified SCF/PEEK at the RS is weaker than that at the AS.

Observing Fig. 7, the microstructures of the Al anchor at the thermo-mechanically affected zone (TMAZ) are featured by the bended and deformed morphologies due to the thermo-mechanical behavior. Moreover, the carbon fiber also flow upwards with the Al anchor penetrating into the SCF/PEEK under the action of flow stress induced by the material transfer [18]. Besides the Al anchor for the FSLW joint, welding defects, such as cavity, tunnel and so on, easily reduce the joining area between the SCF/PEEK and the AA2060-T8, which are detrimental to the tensile properties of the hybrid joint. At a low rotational velocity of 1400 rpm, the formation of the large Al anchor at the upper side

produces the large cavity defect at the bottom of the SZ. This associates with the loss of the partial softening materials, thus resulting in that the cavity is difficult to be filled with the softening SCF/PEEK polymer. When the rotational velocity reaches 1800 rpm or 2000 rpm, although the material flow can be improved and the size of the Al anchor decreases, the overflowing of the softening SCF/PEEK along the interface between the stationary shoulder and the rotational tool is prone to causing the cavity defect (Figs. 6c and d). These welding defects significantly reduce the joining area between the SCF/PEEK and the AA2060-T8, which is difficult to inhibit the deformation of the Al anchor.

Worth mentioning is that the plastic deformation of the Al alloy induced by shear force can fabricate the crevices and irregularities on the surface of AA2060-T8, as depicted in Fig. 8. An intimate contact forms between the SCF/PEEK and the AA2060-T8 under the plunging force applied by the rotational tool, while the crevices and irregularities on the surface of the AA2060-T8 are filled with the re-solidified PEEK and the carbon fiber (white arrows in Fig. 8). Simultaneously, the exposed carbon fibers are entrapped by the plasticized Al (white arrows in Fig. 8). The partial crevices and irregularities are beneficial to increasing the micro-mechanical interlocking between the SCF/PEEK and the AA2060-T8. Fig. 9 depicts the typical interface between the SCF/PEEK and the AA2060-T8 indicating the occurrence of the chemical bonds, which is associated with the Al_2O_3 layer. Okada et al. [23] stated that a part of the oxide layers were decomposed by the hydrolysis to form hydroxyl group which reacted with the functional groups of polymer and raised intermolecular force. Liu et al. [24] employed

plasma electrolytic oxidation (PEO) to deal the surface of magnesium alloy and joined magnesium alloy to poly-ethylene (PE). They stated that high joint strength was attributed to the developments of both chemical bonds at the interface and micro-mechanical interlocking. Therefore, the interfacial joining mechanisms between the SCF/PEEK and the AA2060-T8 are concluded as follows: the macro-mechanical interlocking induced by the Al anchor, the micro-mechanical interlocking by the molten and re-solidified PEEK or carbon fiber into the crevices on the surface of the Al alloy, and the chemical bonds between the SCF/PEEK and the AA2060-T8 due to the chemical radical group and van der Waals force between the PEEK and the Al_2O_3 .

3.3 Mechanical properties

3.3.1 Hardness

The macro-mechanical interlocking induced by the Al anchor exerts the prominent influence on the joint properties. The properties of the Al anchor and its peripheric PEEK are the key. Fig. 10 exhibits the hardness variations of the hybrid joints at different rotational velocities. The average hardness values of the Al anchor gradually decrease with the increase of rotational velocity, which are all lower than the base AA 2060-T8 (174 Hv). The welding peak temperature easily causes the coarse and bended grains in the deformed zone, and then results in a softening region for the heat-treatable Al alloys [25–27]. In this study, the higher the hardness of the Al anchor, the better the ability of the load bearing. For the re-solidified PEEK, the slight hardness variation was observed at the outer of the Al anchor, which is attributed to the reductions of molecular weight and crystallinity. The fast cooling rate is prone to cause the low crystallinity degree. Oliveira

et al. [28] stated that a significant reduction in hardness about 5-10% was caused by the thermal degradation and the reduction in molecular weight. The higher hardness in the re-solidified PEEK is propitious to inhibiting the further deformation of the Al anchor during the tensile shear test and improving the tensile shear load.

3.3.2 Tensile shear properties

Table 1 lists the average values of joining areas of the joint at different rotational velocities, which is used to calculate the tensile shear properties. Load-displacement curves and tensile shear properties of the hybrid joints at different rotational velocities are displayed in Fig. 11. With the increase of rotational velocity, the tensile shear properties of the hybrid joints present increase firstly and decrease. The maximum tensile shear strength of 33 MPa is achieved at the rotational velocity of 1600 rpm. The tensile shear properties are closely corrected with the welding defects, the morphology of the Al anchor and its properties as well as the microstructural evolution of the SCF/PEEK.

To describe the relationships between the surface integrity, the Al anchor (length and hardness), the PEEK hardness, the joint formation and the tensile shear properties, a radar chart is established in Fig. 12. Here, the mechanical properties (tensile shear properties and hardness) and the length of the Al anchor are presented, while the surface integrity and the joint formation (without welding defect) are not quantitative and only graded from the three-dimensional morphology and the macrostructure in cross-section. At 1400 rpm, the partial welding defect easily reduces the joining area and decreases the ability of load bearing, which further results in the lower tensile shear strength compared with that at 1600 rpm. With increasing rotational velocity to 1800 rpm, the Al anchor with small

size and low hardness, and the big welding defect are obtained. These are detrimental to the mechanical interlocking and the load transfer between the SCF/PEEK and the AA2060-T8, which significantly degrade the ability of the load bearing and result in the relatively low tensile shear strength. When rotational velocity reaches 2000 rpm, the hardness and length of the Al anchor drastically reduce, associated with the worse surface integrity and formation (Fig. 12), which consequently lead to the worst tensile shear strength. Moreover, the maximum fracture energy can be achieved at 1600 rpm due to the highest grades of the surface integrity and the joint formation, which reveals the highest toughness of the joint (Fig. 11b). Therefore, the large size of the Al anchor and its high hardness as well as the large chemical bond area at 1600 rpm are all favorable to the tensile shear strength. The relatively high tensile shear strength compared with the papers have been published can also be attained (Fig. 13). The new strategy can achieve the remarkable enhancements of the joint integrity and strength, which may find application in hybrid construction. Meanwhile, in order to further improve the joint strength and fracture toughness, effective surface-pretreatments have been extensively in the fields of adhesive technologies (Table 2). The ultimate aim of these methods is to prevent cracking from epoxy matrix, but also remove the pollutants as well as increase the surface energy and contact area, which all enhance the adhesive strength to a certain extent. Therefore, the surface-pretreatments on the surface of AA2060-T8 or SCF/PEEK need to be investigated in the future work.

3.3.3 Fracture location and fractography

Fig. 14 displays the fracture locations and surface morphologies of the typical hybrid

joint. The macro-morphology of the hybrid joint exhibits the pull-out and fracture of the Al anchor (Figs. 14a~c), while the morphology of the Al anchor presents a big deformation. These means the great ability of load bearing of the Al anchor during tensile shear test. The crack easily initiates during tensile shear test, and the nucleation of fracture path forms after this step. With increasing the tensile shear force, the central crack rapidly propagates along the gap and simultaneously passes through the partial chemical bond area between the SCF/PEEK and the AA2060-T8. Associated with the big deformation of the Al anchor, the final fracture happens when the Al anchor slightly pulls out of the SZ and fracture at the macroscopic level, as exhibited in Fig. 14b. The fracture of the Al anchor is further verified by the EDS, as depicted in Fig. 14c. The fracture surface morphologies of the typical joint are displayed in Figs. 14d~f, which present the both typical characteristics containing the smooth surfaces and the partial coarse surfaces. The formation of the smooth surface is attributed to the crack initiation of the metal/polymer gap and rapid crack propagation, where no sensible plastic deformation occurs, indicating brittle fracture. The dimples induced by the fracture of the Al anchor are observed in Figs. 14d and f, presenting typical ductile fracture, while the other partial coarse surfaces consist of the tearing of the PEEK and pull-out of the carbon fiber. This is attributed to the strong bonding strength and the infiltration of the carbon fiber into the Al alloy or PEEK. This result also conforms to the high tensile shear properties at 1600 rpm.

4. Conclusions

(1) The defect-free joint with the smooth surface finishing was acquired based on the stationary shoulder and the tapered thread pin with the triple facets.

(2) The Al anchor induced by the tapered thread pin with the triple facets formed and directly contacted with the SCF/PEEK, and then avoided the kissing bond. The primary joining mechanisms were attributed to the macro/micro-mechanical interlocking, the chemical bond and the partial infiltration of the carbon fiber into the Al alloy.

(3) With the increase of rotational velocity, the tensile shear properties firstly increased and then decreased. The tensile shear strength reached 33 MPa. The joint fracture presented the pull-out and fracture of the Al anchor, indicating the ductile fracture.

(4) From the viewpoints of the joint surface integrity and strength, friction stir welding with co-controlling shape and performance has become the potential candidate to join thermoplastic and metal instead of the state-of-the-art welding techniques.

(5) Despite this study has achieved the satisfactory results, some limitations need to be addressed. Surface pre-treatments, such as surface patterning, microarc oxidation and so on, need to be explored to further increase the interfacial joining strength between metal and thermoplastic similar to adhesive methods.

Acknowledgements

The work was supported by the National Natural Science Foundation of China (No. 51575132).

References

- [1] Huang Y, Meng X, Xie Y, Wan L, Lv Z, Cao J, et al. Friction stir welding/processing of polymers and polymer matrix composites. *Compos Part A Appl Sci Manuf* 2018;105:235–57. doi:10.1016/j.compositesa.2017.12.005.

- [2] Pramanik A, Basak AK, Dong Y, Sarker PK, Uddin MS, Littlefair G, et al. Joining of carbon fibre reinforced polymer (CFRP) composites and aluminium alloys – A review. *Compos Part A Appl Sci Manuf* 2017;101:1–29. doi:10.1016/j.compositesa.2017.06.007.
- [3] Kim K, Jung YC, Kim SY, Yang BJ, Kim J. Adhesion enhancement and damage protection for carbon fiber-reinforced polymer (CFRP) composites via silica particle coating. *Compos Part A Appl Sci Manuf* 2018;109:105–14. doi:https://doi.org/10.1016/j.compositesa.2018.02.042.
- [4] Tracy J, Yin Y, Yang J, Osborne JC, Blohowiak KY, Dauskardt R. Environmentally assisted crack growth in adhesively bonded composite joints. *Compos Part A Appl Sci Manuf* 2017;102:368–77. doi:https://doi.org/10.1016/j.compositesa.2017.08.018.
- [5] Lionetto F, Mele C, Leo P, D'Ostuni S, Balle F, Maffezzoli A. Ultrasonic spot welding of carbon fiber reinforced epoxy composites to aluminum: mechanical and electrochemical characterization. *Compos Part B Eng* 2018;144:134–42. doi:10.1016/j.compositesb.2018.02.026.
- [6] Lionetto F, Morillas MN, Pappadà S, Buccoliero G, Fernandez Villegas I, Maffezzoli A. Hybrid welding of carbon-fiber reinforced epoxy based composites. *Compos Part A Appl Sci Manuf* 2018;104:32–40. doi:10.1016/j.compositesa.2017.10.021.
- [7] Tan X, Zhang J, Shan J, Yang S, Ren J. Characteristics and formation mechanism of porosities in CFRP during laser joining of CFRP and steel. *Compos Part B Eng* 2015;70:35–43. doi:10.1016/j.compositesb.2014.10.023.
- [8] Huang Y, Meng X, Xie Y, Lv Z, Wan L, Cao J, et al. Friction spot welding of carbon fiber-reinforced polyetherimide laminate. *Compos Struct*

- 2018;189:627–34. doi:10.1016/j.compstruct.2018.02.004.
- [9] André NM, Goushegir SM, dos Santos JF, Canto LB, Amancio-Filho ST. Friction Spot Joining of aluminum alloy 2024-T3 and carbon-fiber-reinforced poly(phenylene sulfide) laminate with additional PPS film interlayer: Microstructure, mechanical strength and failure mechanisms. *Compos Part B Eng* 2016;94:197–208. doi:10.1016/j.compositesb.2016.03.011.
- [10] Rahmat SM, Hamdi M, Yusof F, Moshwan R. Preliminary study on the feasibility of friction stir welding in 7075 aluminium alloy and polycarbonate sheet. *Mater Res Innov* 2014;18:S6-515-S6-519. doi:10.1179/1432891714Z.0000000001035.
- [11] Liu FC, Liao J, Nakata K. Joining of metal to plastic using friction lap welding. *Mater Des* 2014;54:236–44. doi:10.1016/j.matdes.2013.08.056.
- [12] Nagatsuka K, Yoshida S, Tsuchiya A, Nakata K. Direct joining of carbon-fiber-reinforced plastic to an aluminum alloy using friction lap joining. *Compos Part B Eng* 2015;73:82–8. doi:10.1016/j.compositesb.2014.12.029.
- [13] Ratanathavorn W, Melander A. Dissimilar joining between aluminium alloy (AA 6111) and thermoplastics using friction stir welding. *Sci Technol Weld Join* 2015;20:222–8. doi:10.1179/1362171814Y.00000000276.
- [14] Shahmiri H, Movahedi M, Kokabi AH. Friction stir lap joining of aluminium alloy to polypropylene sheets. *Sci Technol Weld Join* 2017;22:120–6. doi:10.1080/13621718.2016.1204171.
- [15] Derazkola HA, Khodabakhshi F, Simchi A. Friction-stir lap-joining of aluminium-magnesium/poly-methyl-methacrylate hybrid structures: thermo-mechanical modelling and experimental feasibility study. *Sci Technol Weld Join* 2018;23:35–49. doi:10.1080/13621718.2017.1323441.
- [16] Panneerselvam K, Lenin K. Joining of Nylon 6 plate by friction stir welding

- process using threaded pin profile. *Mater Des* 2014;53:302–7.
doi:10.1016/j.matdes.2013.07.017.
- [17] Payganeh GH, Arab NBM, Asl YD, Ghasemi F a., Boroujeni MS. Effects of friction stir welding process parameters on appearance and strength of polypropylene composite welds. *Int J Phys Sci* 2011;6:4595–601.
doi:10.5897/IJPS11.866.
- [18] Huang Y, Meng X, Wang Y, Xie Y, Zhou L. Joining of aluminum alloy and polymer via friction stir lap welding. *J Mater Process Technol* 2018;257:148–54.
doi:10.1016/j.jmatprotec.2018.02.043.
- [19] Adhesives - Determination of tensile lap-shear strength of bonded assemblies; English version of DIN EN 1465:2009-07 n.d.
- [20] Ji S, Meng X, Liu Z, Huang R, Li Z. Dissimilar friction stir welding of 6061 aluminum alloy and AZ31 magnesium alloy assisted with ultrasonic. *Mater Lett* 2017;201:173–6. doi:10.1016/j.matlet.2017.05.011.
- [21] Huang Y, Xie Y, Meng X, Lv Z, Cao J. Numerical design of high depth-to-width ratio friction stir welding. *J Mater Process Technol* 2018;252:233–41.
doi:10.1016/j.jmatprotec.2017.09.029.
- [22] Simões F, Rodrigues DM. Material flow and thermo-mechanical conditions during Friction Stir Welding of polymers: Literature review, experimental results and empirical analysis. *Mater Des* 2014;59:344–51.
doi:10.1016/j.matdes.2013.12.038.
- [23] Okada T, Uchida S, Nakata K. Effect of anodizing on direct joining properties of aluminium alloy and plastic sheets by friction lap joining. *Weld Int* 2017;796:1–10.
doi:10.1080/09507116.2017.1346893.
- [24] Liu FC, Liao J, Gao Y, Nakata K. Effect of plasma electrolytic oxidation coating

- on joining metal to plastic. *Sci Technol Weld Join* 2015;20:291–6.
doi:10.1179/1362171815Y.0000000012.
- [25] Chen Y, Liu H, Feng J. Friction stir welding characteristics of different heat-treated-state 2219 aluminum alloy plates. *Mater Sci Eng A* 2006;420:21–5.
doi:10.1016/j.msea.2006.01.029.
- [26] Liu HJ, Fujii H, Maeda M, Nogi K. Tensile properties and fracture locations of friction-stir-welded joints of 2017-T351 aluminum alloy. *J Mater Process Technol* 2003;142:692–6. doi:10.1016/S0924-0136(03)00806-9.
- [27] Huang YX, Wan L, Lv SX, Feng JC. Novel design of tool for joining hollow extrusion by friction stir welding. *Sci Technol Weld Join* 2013;18:239–46.
doi:10.1179/1362171812Y.0000000096.
- [28] Oliveira PHF, Amancio-Filho ST, dos Santos JF, Hage E. Preliminary study on the feasibility of friction spot welding in PMMA. *Mater Lett* 2010;64:2098–101.
doi:10.1016/j.matlet.2010.06.050.
- [29] Augustin T, Karsten J, Kötter B, Fiedler B. Health monitoring of scarfed CFRP joints under cyclic loading via electrical resistance measurements using carbon nanotube modified adhesive films. *Compos Part A Appl Sci Manuf* 2018;105:150–5. doi:10.1016/j.compositesa.2017.11.015.
- [30] Khashaba UA, Aljinaidi AA, Hamed MA. Analysis of adhesively bonded CFRE composite scarf joints modified with MWCNTs. *Compos Part A Appl Sci Manuf* 2015;71:59–71. doi:10.1016/j.compositesa.2015.01.004.
- [31] Lionetto F, Frigione M. Environmental effects on the adhesion properties of nanostructured epoxy-silica hybrids. *J Appl Polym Sci* 2015;132.
doi:10.1002/app.42514.
- [32] Bénard Q, Fois M, Grisel M. Peel ply surface treatment for composite assemblies:

- Chemistry and morphology effects. *Compos Part A Appl Sci Manuf* 2005;36:1562–8. doi:10.1016/j.compositesa.2005.02.012.
- [33] Li J, Li Y, Huang M, Xiang Y, Liao Y. Improvement of aluminum lithium alloy adhesion performance based on sandblasting techniques. *Int J Adhes Adhes* 2018;84:307–16. doi:10.1016/j.ijadhadh.2018.04.007.
- [34] Reitz V, Meinhard D, Ruck S, Riegel H, Knoblauch V. A comparison of IR- and UV-laser pretreatment to increase the bonding strength of adhesively joined aluminum/CFRP components. *Compos Part A Appl Sci Manuf* 2017;96:18–27. doi:10.1016/j.compositesa.2017.02.014.
- [35] Tao R, Alfano M, Lubineau G. Laser-based surface patterning of composite plates for improved secondary adhesive bonding. *Compos Part A Appl Sci Manuf* 2018;109:84–94. doi:10.1016/j.compositesa.2018.02.041.
- [36] Palmieri FL, Belcher MA, Wohl CJ, Blohowiak KY, Connell JW. Laser ablation surface preparation for adhesive bonding of carbon fiber reinforced epoxy composites. *Int J Adhes Adhes* 2016;68:95–101. doi:10.1016/j.ijadhadh.2016.02.007.
- [37] Sánchez Serrano J, Ureña A, Lazcano Ureña S, Blanco Varela T. New approach to surface preparation for adhesive bonding of aeronautical composites: Atmospheric pressure plasma. Studies on the pretreatment lifetime and durability of the bondline. *Compos Interfaces* 2015;22:731–42. doi:10.1080/09276440.2015.1056671.
- [38] Okada T, Kanda M, Faudree MC, Nishi Y. Shear strength of adhesive lamination joint of aluminum and CFRP sheets treated by homogeneous low energy electron beam irradiation prior to lamination assembly and hot-press. *Mater Trans* 2014;55:1587–90. doi:10.2320/matertrans.MAW201419.

- [39] Hao X, Wang H, Hua L, Zhou H, Lei S. Study on the law of ultrasonic vibration-assisted adhesive bonding of CFRP-to-Aluminum joints. *Int Conf Mech Mechatronics Eng* 2017:239–45.

Figure captions

Fig. 1 Schematic illustration for the FSLW based on the novel welding configuration.

Fig. 2 Locations of the metallurgical and mechanical specimens.

Fig. 3 Schematic diagram for the tensile shear test of the hybrid joint.

Fig. 4 Surface integrity of the typical joint.

Fig. 5 Three-dimensional morphologies of the joints obtained by different rotational velocities: (a) 1400 rpm, (b) 1600 rpm, (c) 1800 rpm and (d) 2000 rpm.

Fig. 6 Macrostructures in cross-section of typical joints at different rotational velocities: (a) 1400 rpm, (b) 1600 rpm, (c) 1800 rpm and (d) 2000 rpm. (The yellow presents the SCF/PEEK; the green depicts the defect; the orange means the AA2060-T8)

Fig. 7 Material spreading at the AS and RS near the Al anchor: (a) AS and (b) RS.

Fig. 8 Micro-mechanical interlocking and infiltration of carbon into Al matrix.

Fig. 9 Interface characteristics: (a) SEM view and (b) distribution of Al element.

Fig. 10 Hardness of the typical locations for the Al anchor and its surrounding PEEK.

Fig. 11 (a) Force-displacement curves and (b) tensile shear properties of the joints.

Fig. 12 Radar chart of the microstructural characteristics versus mechanical properties.

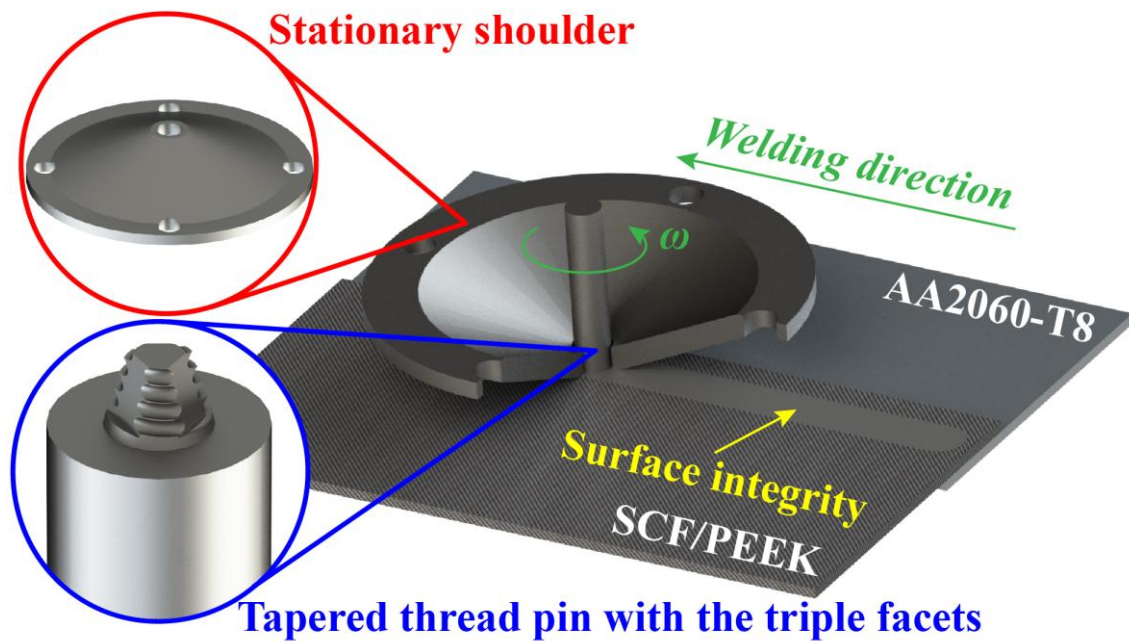
Fig. 13 Maximum shear strength of the joints by different methods.

Fig. 14 Fracture surface morphologies: (a) macro-morphology, (b) enlarged view by square in Fig. 14a, (c) distribution of Al element; (d) d, (e) e and (f) f in Fig. 14b.

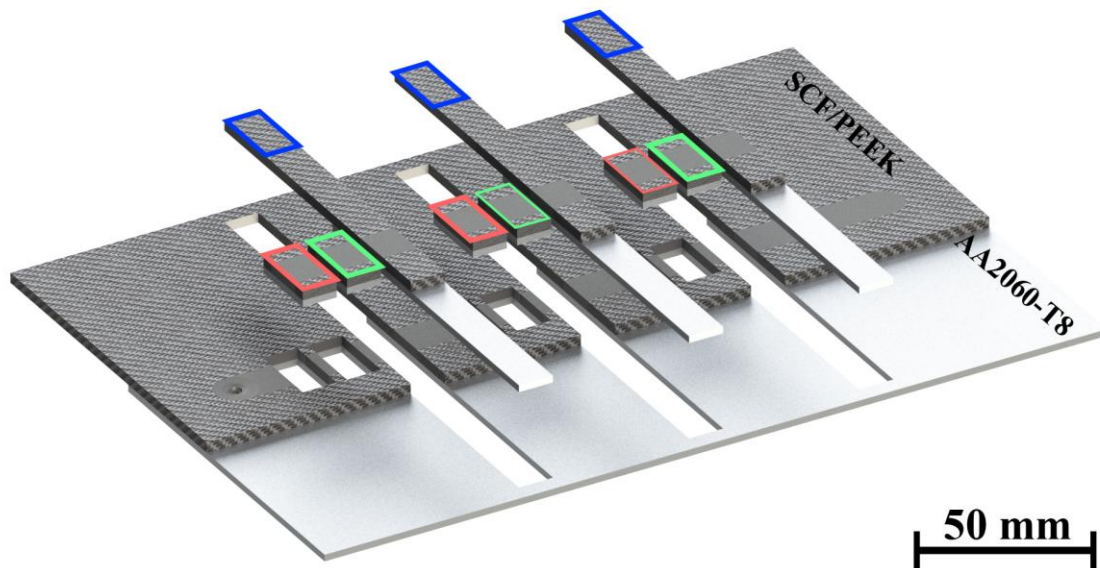
Table captions

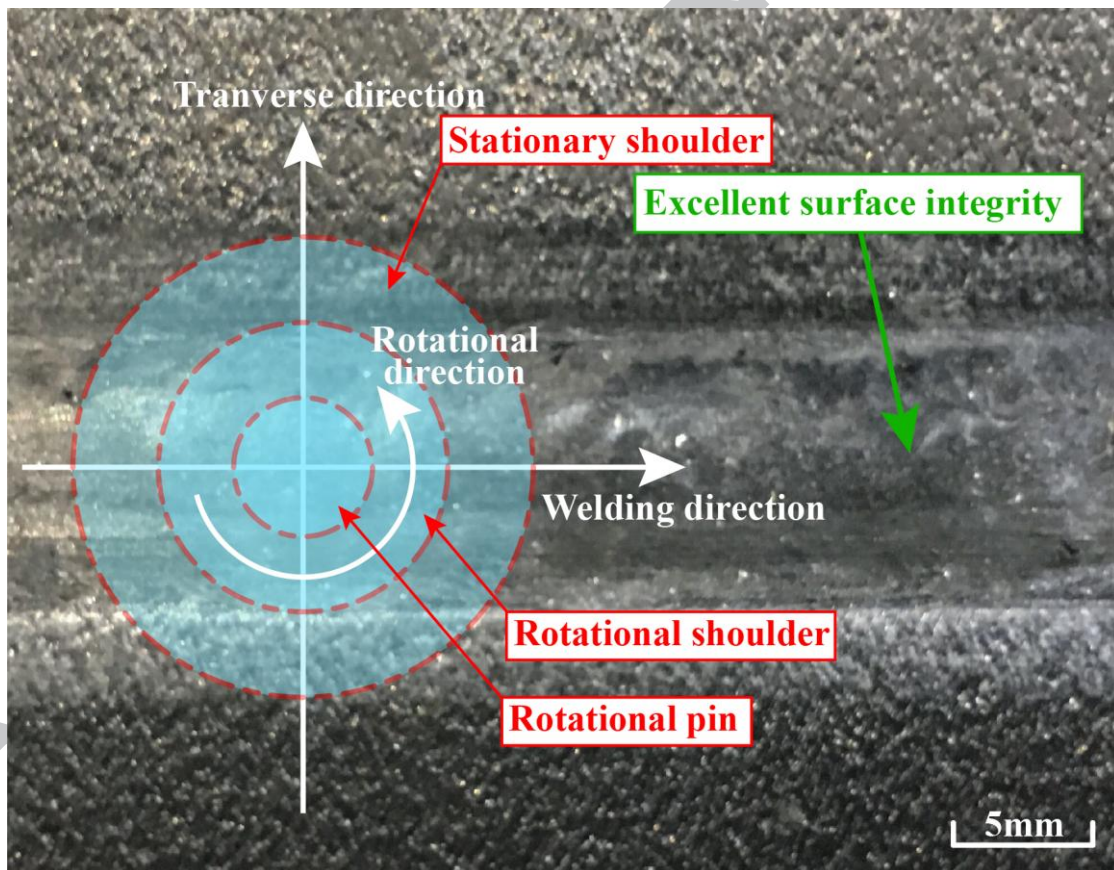
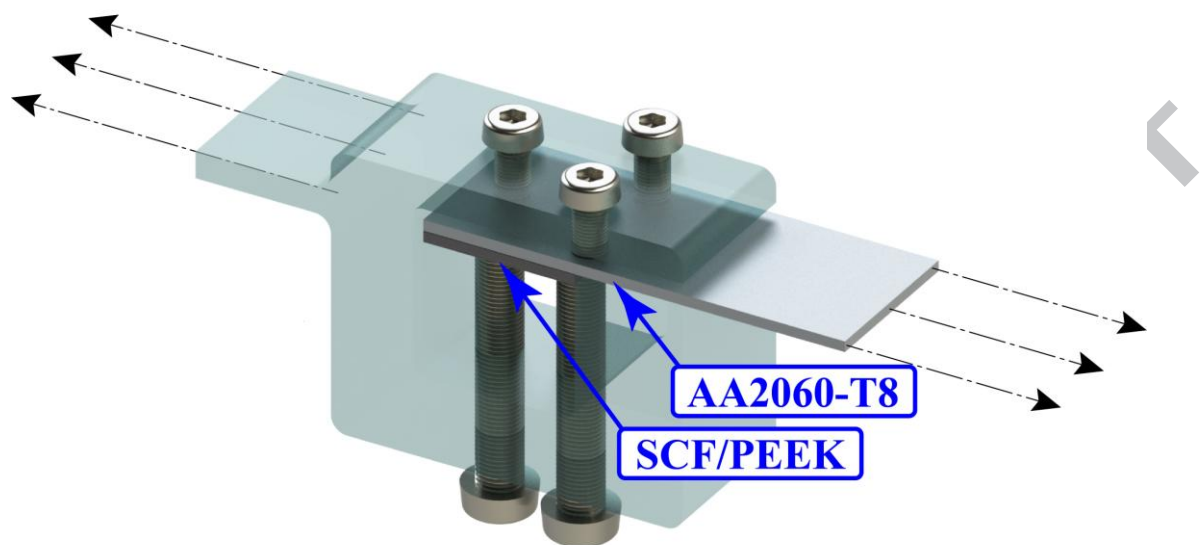
Table 1 Average values and standard deviations of the joining areas.

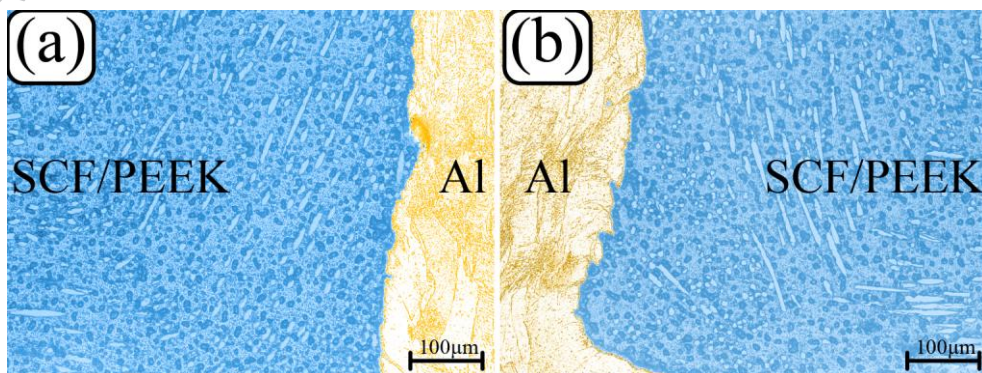
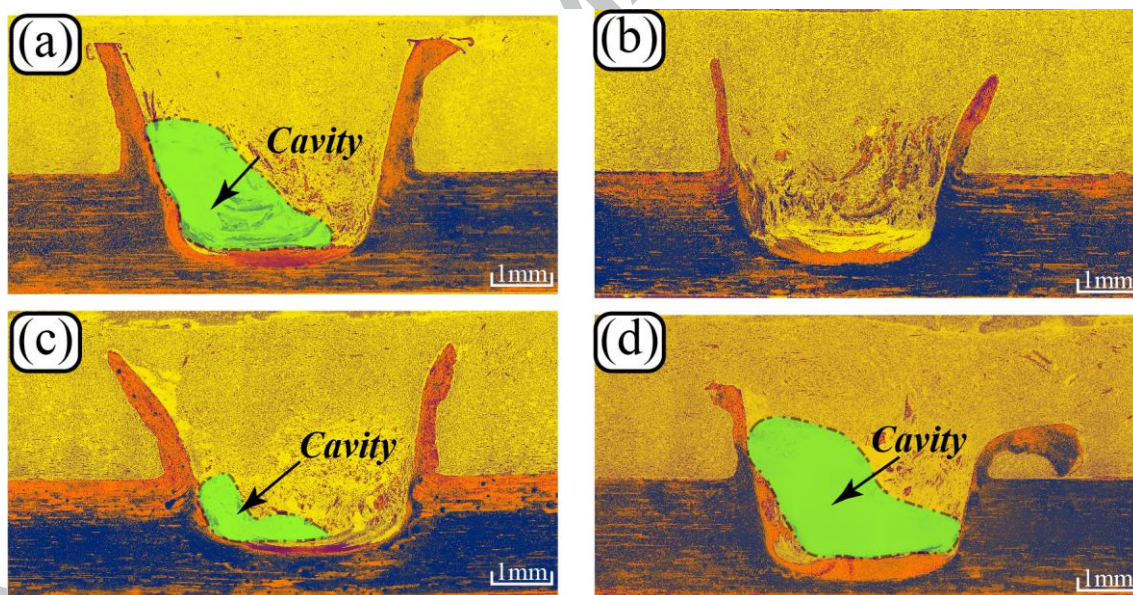
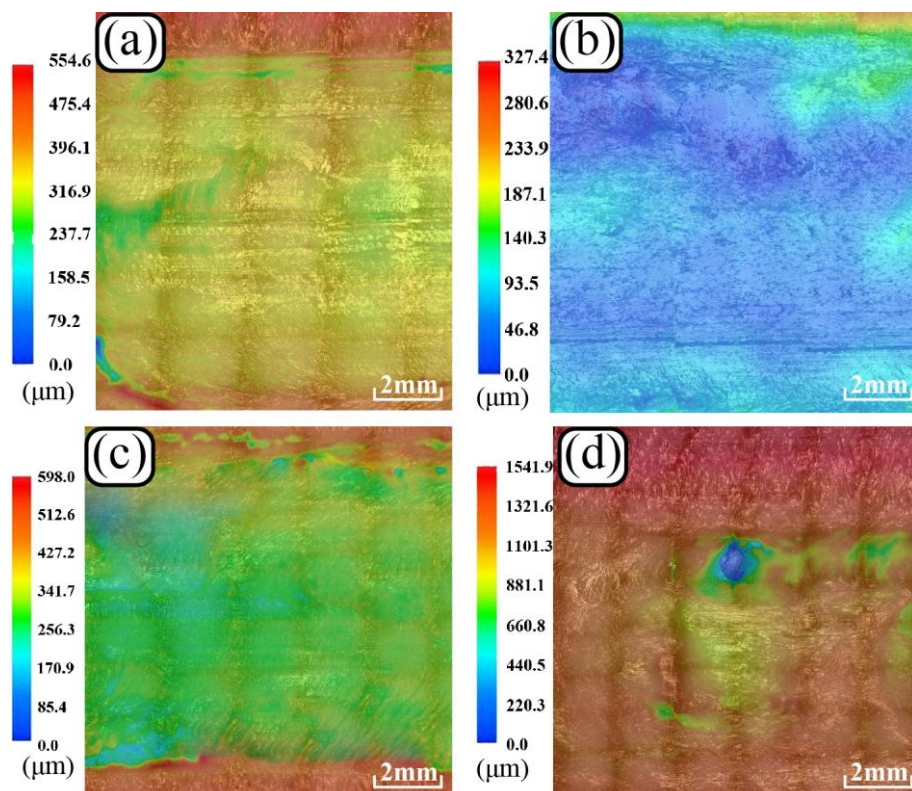
Table 2 Existing studied methods to improve adhesive strength.

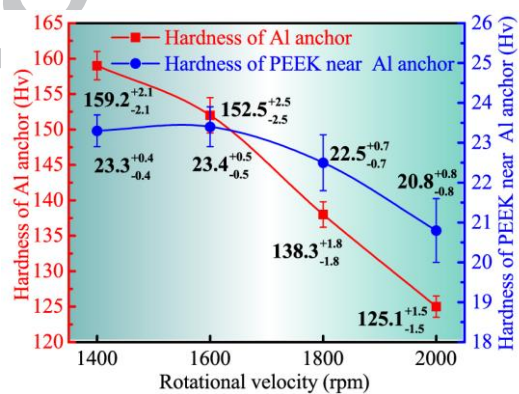
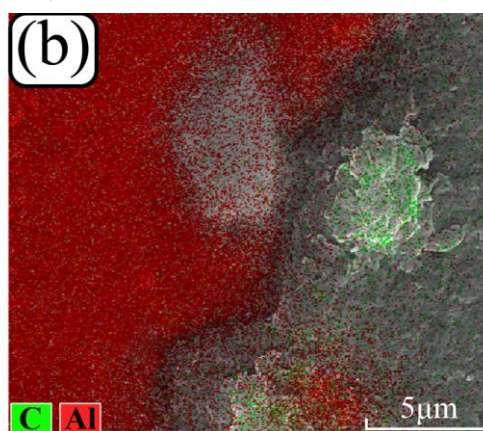
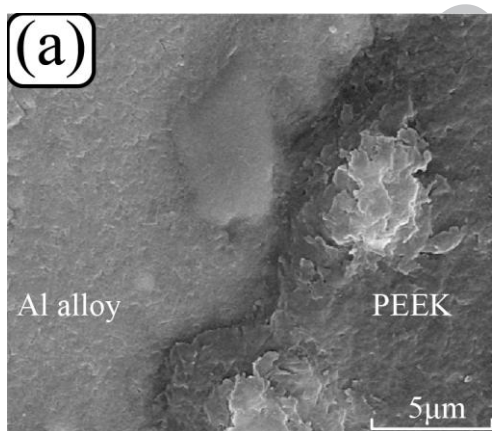
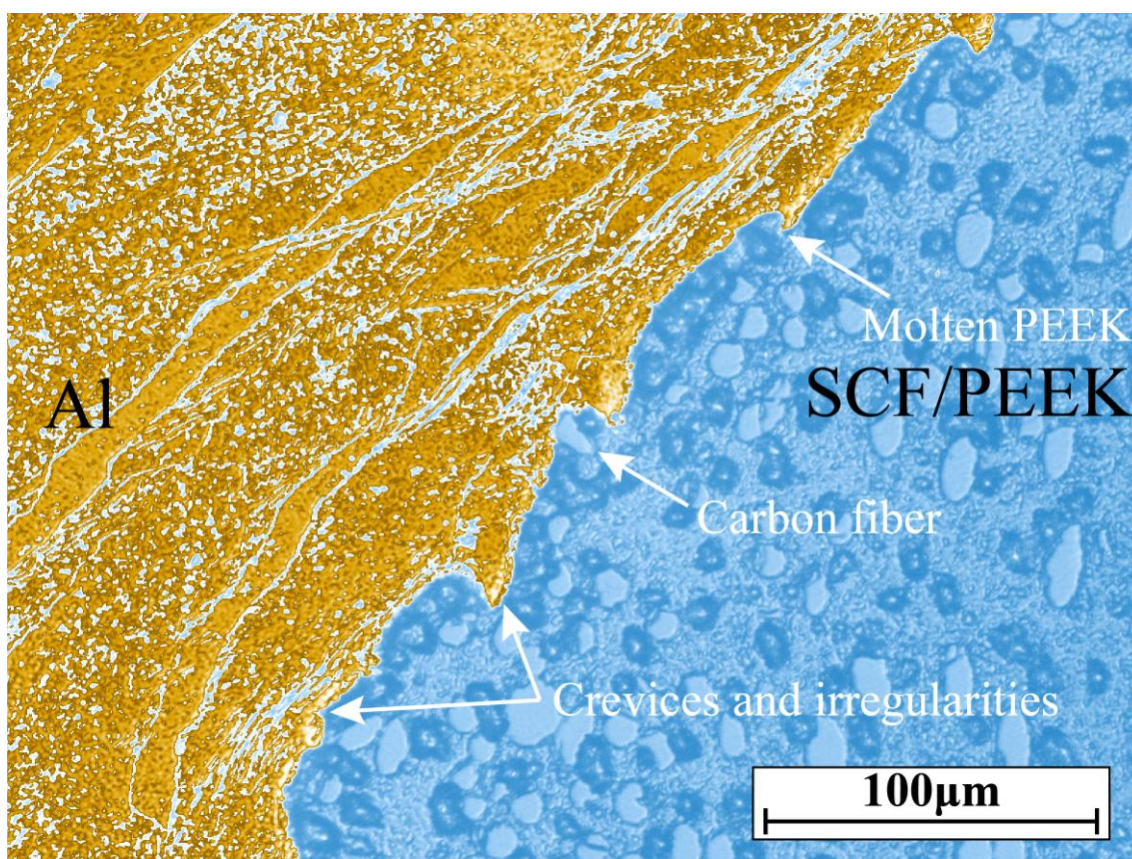


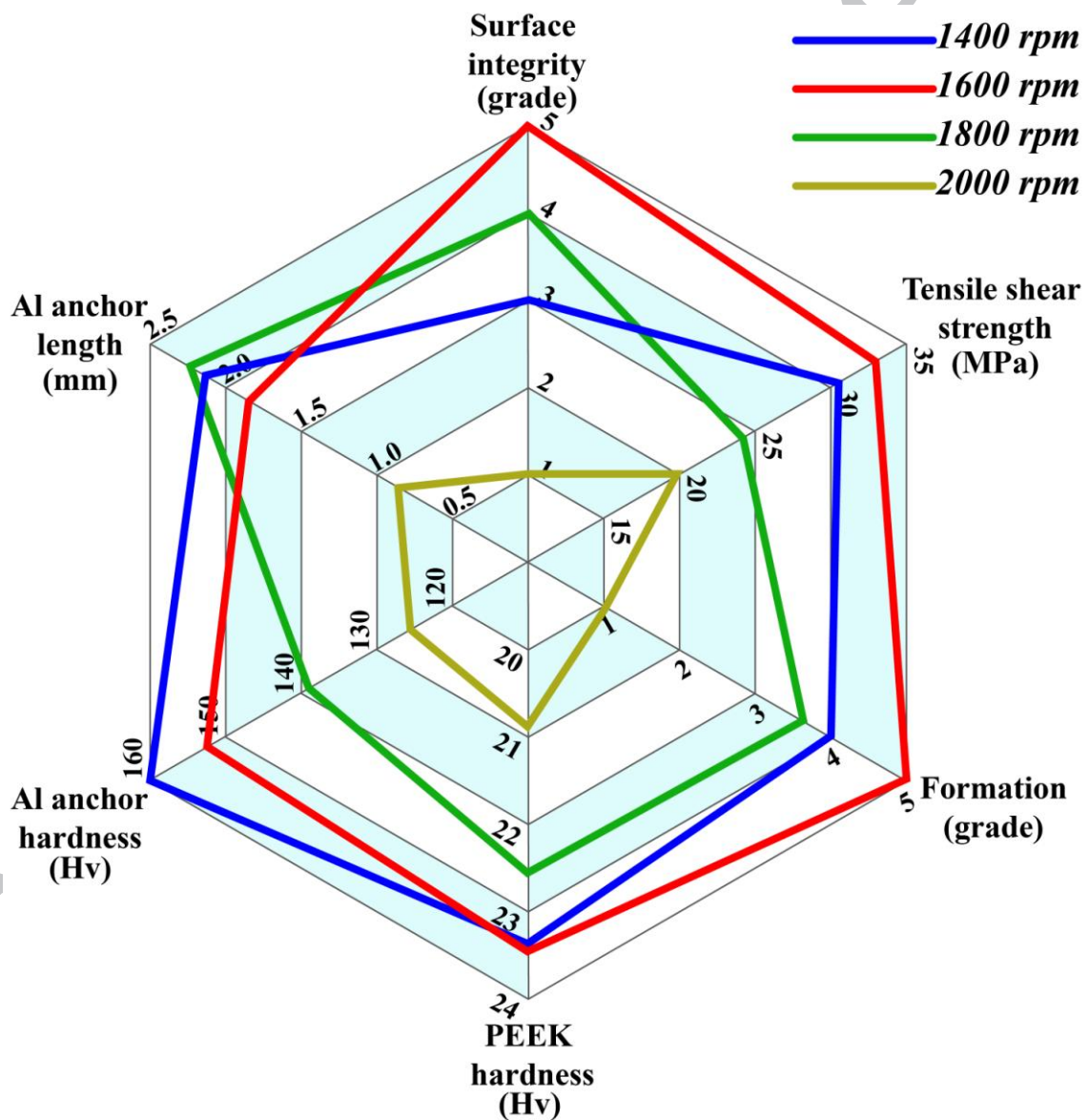
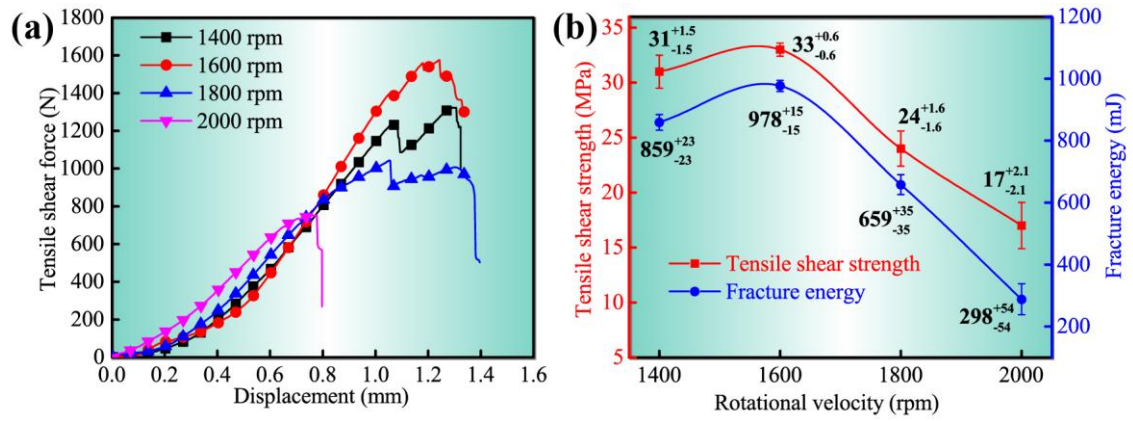
Tensile shear specimens Microhardness specimens Metallographic specimens











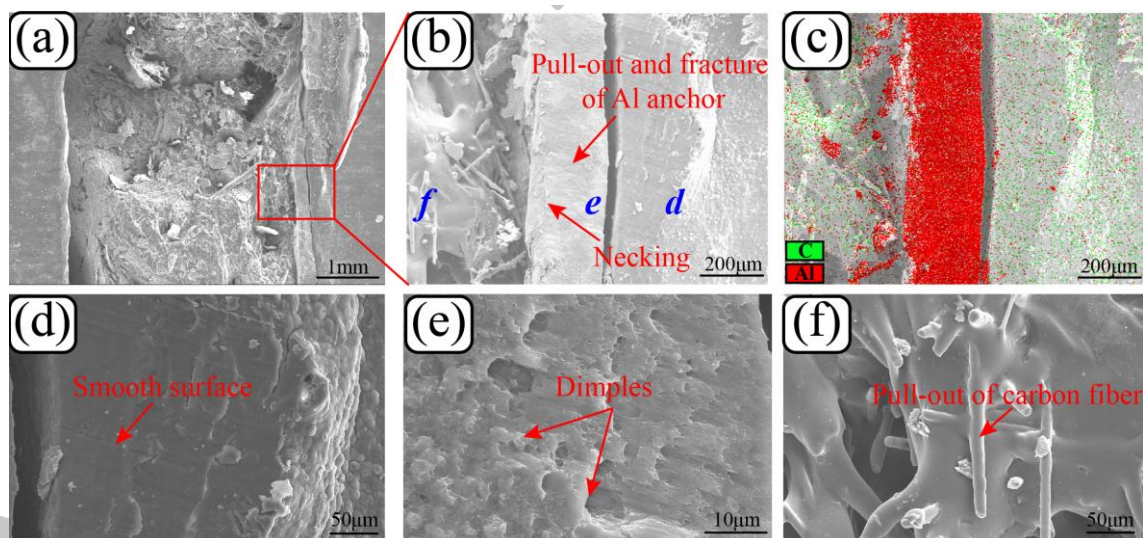
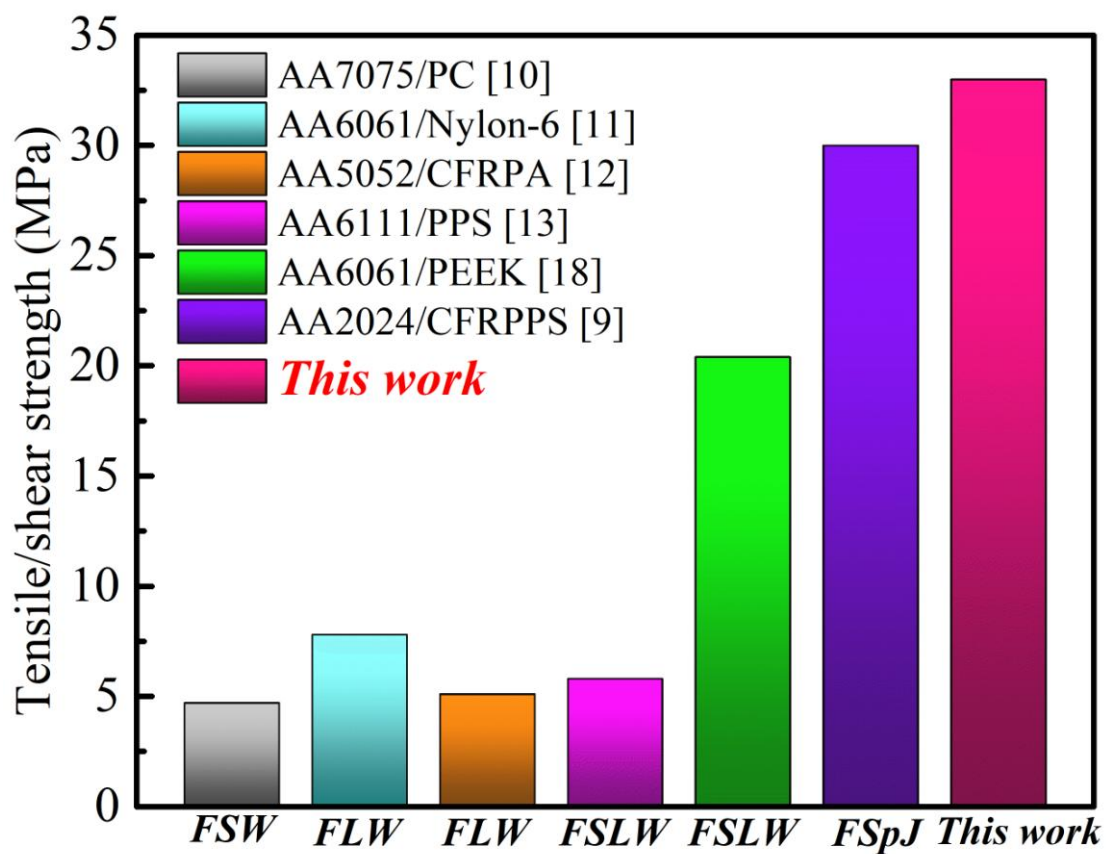


Table 1 Mean values and standard deviations of the joining areas.

Rotational velocity (rpm)	Specimen	Average value (mm ²)	Standard deviation
1400	1	43.5	0.2
	2	44.5	0.3
	3	43.1	0.2
1600	1	47.9	0.2
	2	47.3	0.4
	3	47.1	0.2
1800	1	43.2	0.4
	2	44.8	0.3
	3	43.8	0.2
2000	1	41.4	0.2
	2	41.0	0.4
	3	41.0	0.5

ACCEPTED MANUSCRIPT

Table 2 Existing studied methods to improve adhesive strength

Pre-treatment	Effect	References
Carbon nanotube filler	Prevent cracking from epoxy matrix	[29,30]
Silica particle filler		[3,31]
Peel-ply	Remove pollutants, and increase the surface polarity, surface energy, and contact area	[32]
Mechanical sandblasting		[33]
Laser-based surface patterning:	Remove pollutants on the adhesive surface and improve the contact area through pattern or structure formation	
IR/UV		[34]
CO ₂		[35]
Nd: YAG		[36]
Vapor pressurized plasma	Increase binding energy between metal and polymer, and promote covalent bonding	[37]
Homogeneous low-energy electron beam irradiation		[38]
Ultrasonic vibration	Promote the adhesive to penetrate into the contact surface structure	[39]